THE PENNSYLVANIA STATE UNIVERSITY
SCHREYER HONORS COLLEGE

DEPARTMENT OF MATERIALS SCIENCE AND ENGINEERING

Investigation and Manipulation of Structural Color Produced from Microscale Concave Interfaces in Fluid and Solid Systems

AMANDA GREGG
SPRING 2022

A thesis
submitted in partial fulfillment
of the requirements
for a baccalaureate degree
in Materials Science and Engineering
with honors in Materials Science and Engineering

Reviewed and approved* by the following:

Lauren Zarzar
Assistant Professor of Chemistry
Thesis Supervisor

Robert Allen Kimel
Associate Teaching Professor of Materials Science and Engineering
Honors Adviser

* Electronic approvals are on file.

ABSTRACT

Structural color via total internal reflection at microscale concave interfaces was studied to contribute to the fundamental understanding of this novel mechanism of structural color. Additionally, potential applications for the technology were explored. First, color in double emulsion droplets was investigated, as the phenomenon was not expected in droplets of this morphology. As part of this work, molecular models of the droplets were created to better understand and visualize the interactions of the surfactant, oil, and water molecules at the oil-water interface as well as spacing between molecules. Droplets were found to a nonideal medium in which to study this color, due to challenges in creating monodisperse droplets, drift of the droplets in the dish, and solubilization of the oil into the aqueous phase. Polymer microstructures were found to be easier to study and fabricate than the droplets, with more directions for study and applications. Since the color produced can be modified by changing the width of the structures, infrared lasing was found to be an effective tool to increase the width and therefore, change the color. Although the deformation needed to modify the color was too small to be measured accurately, it was found that the microstructures can no longer produce color past a 4 μm change in width. These results could be used to create an inkless printing technology for anticounterfeiting features and product design.

TABLE OF CONTENTS

LIST OF FIGURES

LIST OF TABLES

ACKNOWLEDGEMENTS

I would first like to thank my research advisors, Dr. Lauren Zarzar and Dr. Christopher McComb, for supporting me through not only my research but also applying to graduate school and any other school or life advice I needed. The research experiences I had with them allowed me to discover my passion for research and make the decision to obtain my Ph.D. I want to thank Dr. Zarzar for accepting me into her research group after I had only completed one semester of college and for helping to facilitate a supportive and friendly lab culture. I also want to thank Dr. McComb for accepting me into the Penn State College of Engineering REU program when I had no previous experience in the research topic and had only learned to code the semester before. I want to thank him also for continuing to support my research after taking a position at another university. Thank you again to both of my research advisors for providing me an incredibly positive undergraduate research experience.

Next, I would like to thank my friends and family for their unconditional support. Thank you to my parents for raising me to be motivated, curious, and have a wide range of interests. Thank you also for everything you did for me to allow me to focus on my education, from saving for my tuition to sending me back after breaks with leftovers and homemade bread. I am so appreciative also to my close friends and lab group for always being there for me, for your advice, and for all the fun memories – I will miss you all so much. I want to separately thank my lab group members for helping me to set up experiments and fabricate samples.

Lastly, I want to thank the Department of Materials Science and Engineering, College of Earth and Mineral Sciences, Schreyer Honors College, and Provost Dr. Nicholas Jones for awarding me scholarships throughout my time at Penn State. Thanks to your help, I can go on to obtain my Ph.D. without worry of having to pay back student debt.

This research was partially funded by NSF Grant IIP-2016420. The findings and conclusions do not necessarily reflect the views of the funding agency.

Background on Structural Color

Structural color is produced when light interacts with structures in a material. The color is a result of interference of the waves of light that entered the material. Common examples are soap bubbles, opals, and butterfly wings. This optical phenomenon is of interest to researchers due to its prevalence in biology and nature, so understanding the mechanisms by which it is produced will help scientists to reproduce them synthetically for applications in aesthetic design [1] and security features [2]. Additionally, it is worth noting that structural color produces brilliant, vibrant colors that are beautiful and enjoyable to study. This simple aspect of color research should not be overlooked and is a legitimate motivation for studying structural color. This chapter will discuss the main known mechanisms of structural color to provide background and context to structural color at the microscale, which is the mechanism that was studied in this thesis. It will then conclude with an in-depth explanation of structural color on the microscale.

Thin-Film Reflection and Interference

The underlying mechanism of structural color and reflection due to thin films is light passing through a high-refractive index material backed with a low-refractive index material [1,3]. A portion of the incident light will be reflected back to the observer, which depends on the incident light angle [3]. The exiting light rays, depending on the refractive index and thickness of the high-index layer, will constructively and/or destructively interfere [3,4]. This interference occurs due to an increase in path length of the wave as it travels through the high-index layer. To

observe color, those wavelengths for a particular color, red for example, must constructively interfere, and the others must experience destructive interference [3].

A characteristic feature of structural color is its iridescence, which means that the observed color changes with viewing angle. This phenomenon is illustrated by the condition for constructive interference (equation 1) [1]:

$$2n_{film}dcos\theta_{film} = m\lambda \quad (Eq. 1)$$

The refractive index of the film is given by n_{film} and is considered to be backed with a material of lower refractive index. The thickness of the film is given by d, and the angle from the normal of the wave propagating through the depth of the film is given by θ_{film}. m is an integer, and λ is the wavelength of light entering the material. Due to the inverse relationship between λ and θ_{film}, as the light's incident angle increases, the outgoing wavelength will decrease, hence giving rise to iridescence [1], illustrated in Figure 1. The upper plot in Figure 1 has one peak for each angle due to the comparatively low film thickness [3]. When only one peak is observed, the color is considered spectral, which means that only one wavelength is observed by the human eye, such as red [3]. However, in the case of the lower plot in Figure 1, multiple peaks were observed due to the comparatively higher film thickness, which allows for multiple reflections [3]. The physical result is that the observer sees non-spectral color, which results from multiple wavelengths being observed at once, such as pink [3].

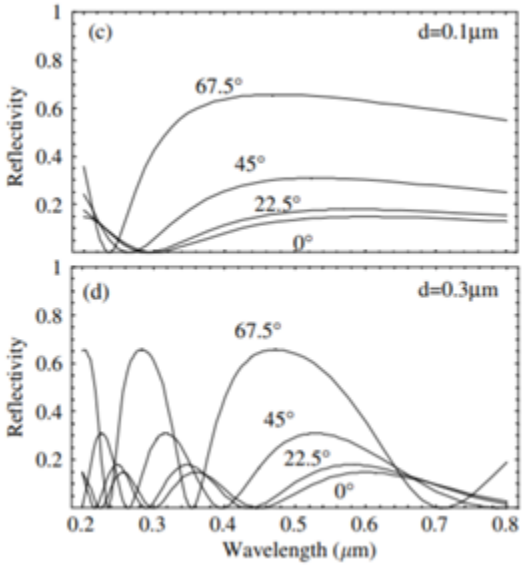

Figure 1. Wavelength vs reflectivity plots for a material of refractive index of 1.5 backed in air showing angle dependence of the color, reproduced from Kinoshita et al. (2008). The upper plot has a film thickness of 0.1μm, and the lower plot has a film thickness of 0.3μm.

This color can be achieved either from either one high-index layer backed with one low-index layer or from multiple high and low index layers stacked [3].

Single-layer Interference

The most common example of single-layer interference is soap bubbles. As mentioned above, in a system with a high to low refractive index change, some portion of the incident light is reflected at the surface while the rest is refracted at the interface between the high and low-refractive index materials. When there is only one layer of high-index material, the structural color observed is due to those reflected and refracted waves interfering [5]. This interference occurs because the light waves that travel through the high-index layer will gain in path length as

compared to those that just reflected off the top surface of the high-index layer [5]. This behavior is illustrated in Figure 2.

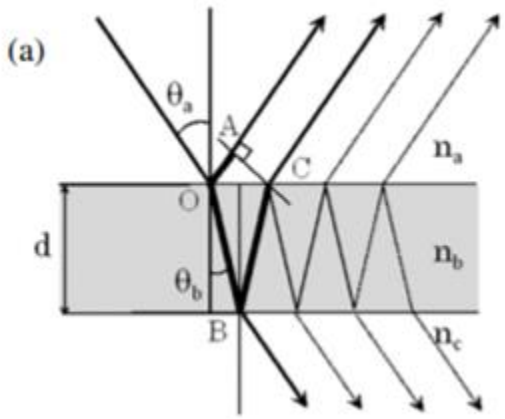

Figure 2. Thin-film interference of a single layer, where $n_b > n_c$, reproduced from Kinoshita et al. (2008).

Jaszkowski and Rzeszut provide equations to quantify this change in path length (Δl) and phase (δ_t) between two waves of light entering the material, where n_2 is the high-refractive index layer, d is the depth of the layer, and θ_2 is the angle from the normal of the incoming light traveling through the high-index layer [5]. In reality, there are multiple beams of light reflecting and refracting multiple times, but these equations are given for simplicity.

$$\Delta l = 2n_2(\lambda)dcos\theta_2 \quad (Eq. 2)$$

$$\delta_t = \frac{4\pi}{\lambda} n_2(\lambda)dcos\theta_2 + \pi \quad (Eq. 3)$$

As shown in equations 2 and 3, the change in path length and phase are both dependent on thickness of the high-index layer. This result is why the colors of a soap film, maybe in one's

dishwater while washing dishes, changes as the film moves around on the surface of the water. To provide quantitative evidence of this phenomenon, Figure 3 displays a plot of different high-index layer thicknesses on the CIE color space.

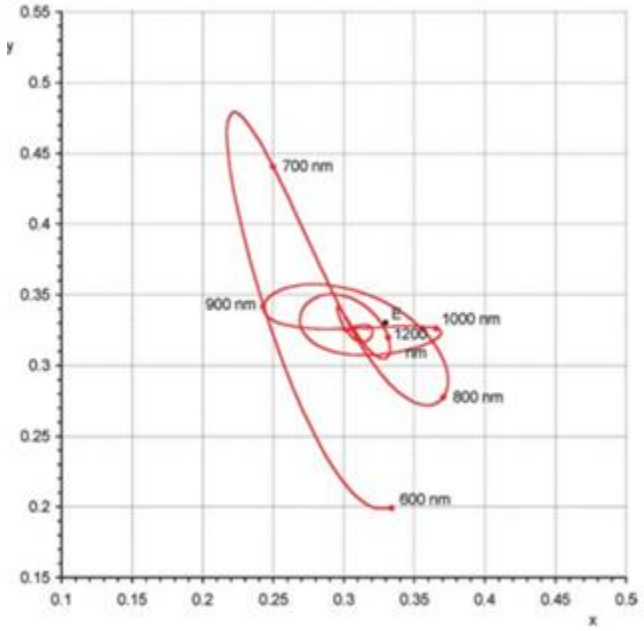

Figure 3. Varying high-index layer thicknesses plotted on CIE color space, where the axes are chromaticity coordinates. Figure reproduced from Jaszkowski and Rzeszut (2003).

Multilayer Interference

By adding multiple high and low refractive index layers, the interaction that light had with the single layer occurs at each layer in the stack [4]. Figure 4 illustrates constructive interference in layers of thin films of alternating high and low refractive indices [4]. If all the wavelengths of all the exiting light waves are perfectly and equally in phase, the reflectance from each layer will continue to build, resulting in a completely reflective surface after so many layers

have been added, usually more than 10 [4]. This type of material is called an “ideal multilayer” [3].

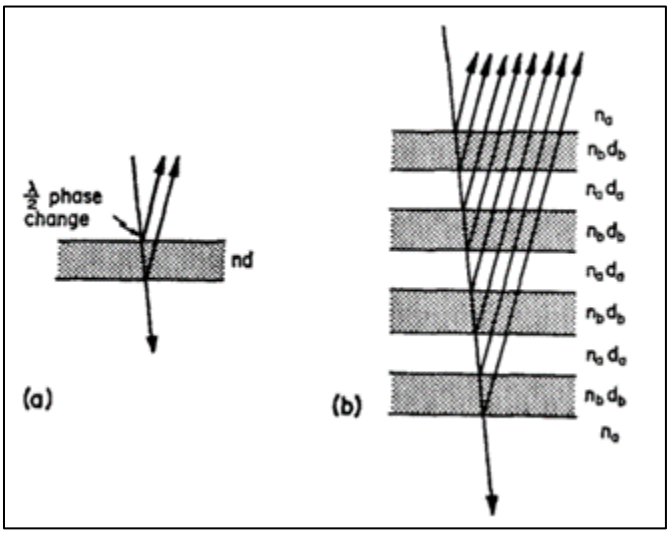

Figure 4. Multilayer reflection, reproduced from Land (1972).

However, if the material does not show constructive interference of all wavelengths of the light equally, colors can result [3]. This material, by contrast, is called a “non-ideal multilayer” [3].

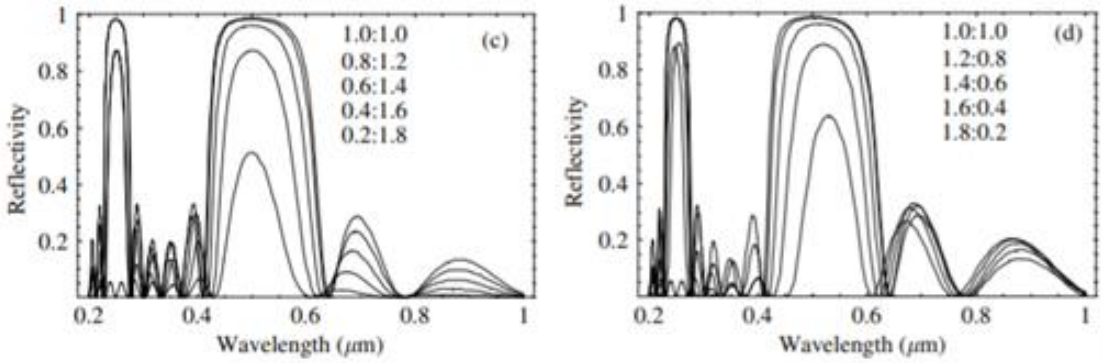

Figure 5. Wavelength vs reflectivity of non-ideal multilayered materials, reproduced from Kinoshita et al. (2008).

Diffraction Gratings

Diffraction gratings interact with light via periodic structures with different refractive indices [7] in the material, where the incoming light is diffracted off the surface of the structures, illustrated in Figure 6 [8].

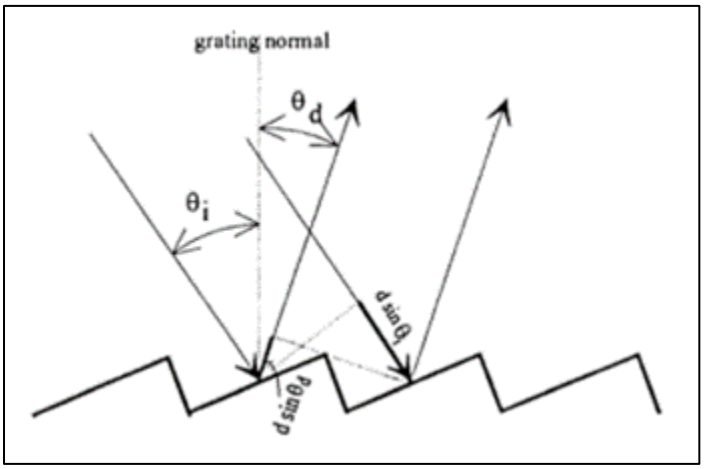

Figure 6. Schematic of a diffraction grating, reproduced from Loewen and Popov (1997).

One can use the grating equation (equation 4) to quantitatively describe the behavior of these materials. θ_m is the angle between the incident light wave and the normal of the surface, θ_i is the angle between the incident light wave and the diffracted wave, m is an integer, and d is the grating period [8].

$$sin\theta_m = sin\theta_i + m\frac{\lambda}{d}, \qquad m = 0, \pm1, \pm2, etc. \quad (Eq. 4)$$

The grating equation is a form of an equation for constructive interference, so only a certain wavelength, λ, will be allowed for a given spacing and incident light angle [7]. Therefore,

one will observe the wavelength as a color since the gratings are designed to have a spacing on the order of visible light [7]. For this reason, diffraction gratings are used to separate and disperse the incident light [7].

Photonic Crystals

Photonic crystals exhibit structural color due to both a high refractive index contrast within the structure as well as a two or three-dimensional structure that cannot be treated as a three-dimensional structure containing one-dimensional planes and atoms [9]. When researchers use X-ray diffraction to analyze crystal samples, they treat the structures as comprised of these one-dimensional planes and atoms [9]. However, photonic crystals are too complex to be treated in this manner [9]. It is useful to compare them to superlattices. Superlattices are layers of two-dimensional materials stacked on top of one another, where the lattice parameter becomes many angstroms thick [10]. Photonic crystals are analogous to these lattices, as layers of crystals with different refractive indices are stacked on top of one another [11]. The lattice constant, however, is much larger than angstroms; it is on the order of the wavelength of electromagnetic waves desired to interact with the material [11]. As illustrated in Figure 7, these crystals can be stacked in one, two, or three dimensions.

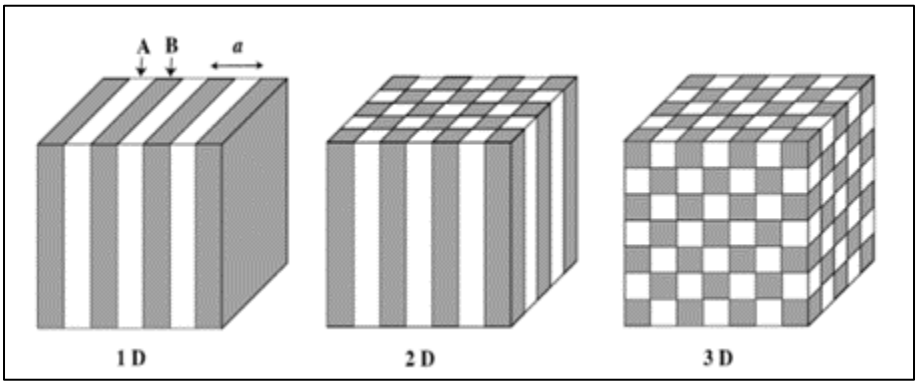

Figure 7. Photonic crystals in one, two, and three dimensions; *a* is the lattice constant. Figure reproduced from Sakoda (2005).

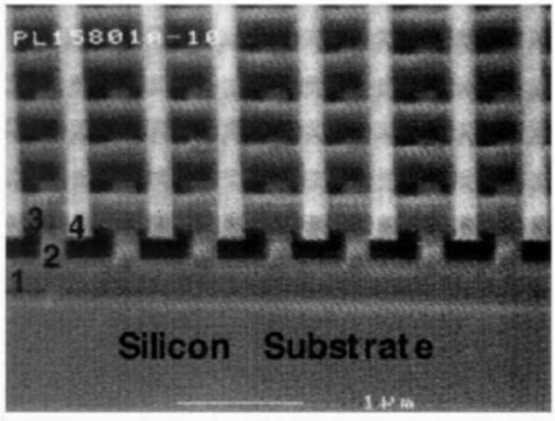

Figure 8. SEM image of a Si three-dimensional photonic crystal, reproduced from Sakoda (2005).

Most research is conducted on two and three-dimensional photonic crystals due to their properties, such as the group-velocity anomaly and nonlinear optics [11]. As described by Sakoda, "the anomalous group velocity takes place when the original wave vector in the uniform material is not parallel to either b1 or b2", where b1 and b2 are the reciprocal lattice vectors of the two-dimensional photonic crystal lattice [11]. The consequence of this non-parallel wave vector is that one band has a smaller group velocity than the others [11]. Considering equation 5 [11], where ω is the angular frequency, and k is the wavevector:

$$v_g = \frac{\partial \omega}{\partial k} \quad (Eq. 5)$$

When $\frac{\partial \omega}{\partial k}$, which is the slope of the band, is small, the group velocity is small. This phenomenon is shown visually by the third band from the bottom along the ΓΔX direction in Figure 9.

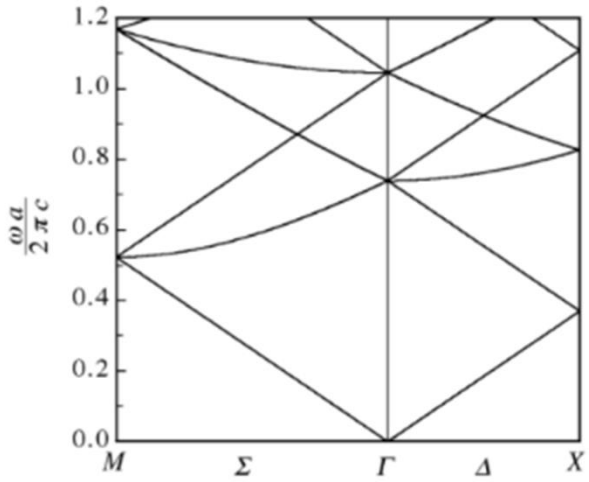

Figure 9. Wave vectors in the first Brillouin zone of a two-dimensional photonic crystal, reproduced from Sakoda (2005).

Physically, this small group velocity has results in the material such as greater light absorption and stimulated emission [11]. The enhanced nonlinear optical properties in photonic crystals result from the fact that the final wavevector is not equal to the initial wavevector [11].

Light Scattering

Light scattering is simply the phenomenon of light waves interacting with tiny particles that scatter the waves [12]. Arguably the most well-known scattering theory is Mie Theory, published by Gustav Mie in 1908 [13]. This theory describes the light scattering of plane waves by a homogeneous, isotropic, dielectric sphere [13]. The rainbow is a common example of this phenomenon [14]. Rainbows result from scattering from particles ~ 1000 µm in diameter within a few degrees of light [14]. These angles are directly dependent on refractive index, so it can be concluded that the colors of a rainbow are dependent on variations in refractive index across the visible portion of the electromagnetic spectrum [14]. Figure 10 provides a graphical representation of Mie Theory for droplets of various sizes. The optical phenomena of glories and coronas are also shown on the plot.

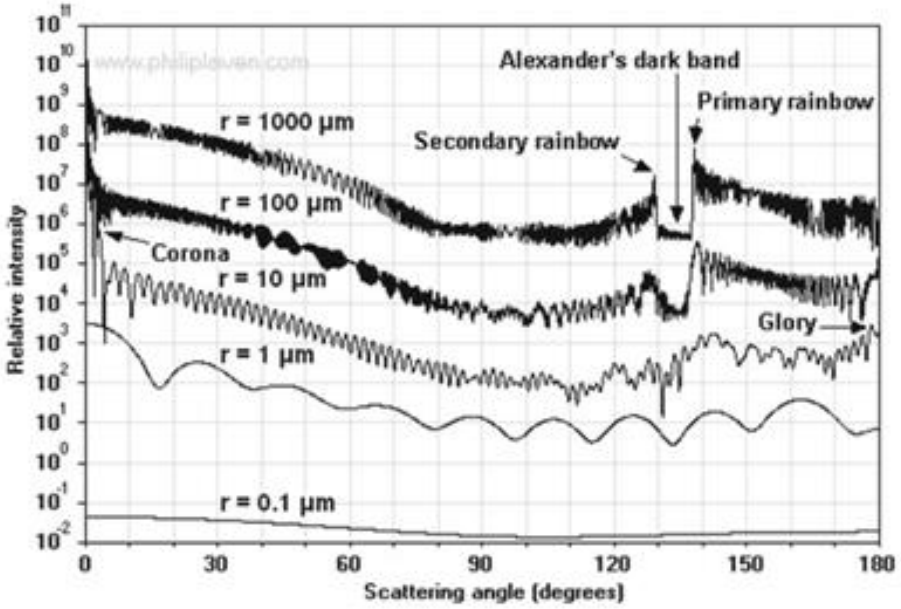

Figure 10. Mie theory applied to spherical water droplets of varying sizes (r = 0.1 µm to r = 1000 µm) when interacting with incident unpolarized monochromatic light of wavelength 650 nm. Figure reproduced from Laven (2012).

Other light scattering theories exist to describe different shapes and types of droplets, although they will not be mentioned here. A description of Mie theory was provided to illustrate the general concept of light scattering from small particles, so a discussion of the other theories is not necessary.

Structural Color via Total Internal Reflection

The newest mechanism of structural color, and the one that will be the focus of this thesis, was published in 2019 by members of the Zarzar lab. The mechanism produces color via total internal reflection at microscale concave interfaces [6]. As mentioned earlier in this report, when light that is traveling through a material of high refractive index meets a layer of lower refractive index, some portion of the light is reflected. If the incident light angle reaches a critical point, all the light is reflected; this phenomenon is called total internal reflection [6]. If the interface between the high and low-index materials has a concave structure, the totally-internally reflected light will bounce along the interface until the light exits the structure [6]. As shown in Figure 11, each light ray experiences a different number of bounces, which causes the path lengths of the outgoing light to be changed relative to the incident light [6]. This change in path length causes the waves to interfere as they do thin-film interference, resulting in color. This phenomenon is demonstrated in Figure 12.

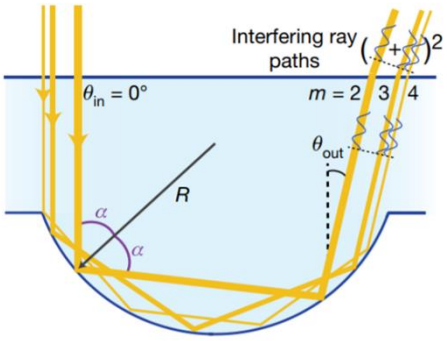

Figure 11. Rays of light experiencing total internal reflection along the concave interface between the two oils in a Janus droplet. Each ray of light bounces a different number of times along the interface, resulting in interference of the outgoing rays. Figure reproduced from Goodling et al. (2019).

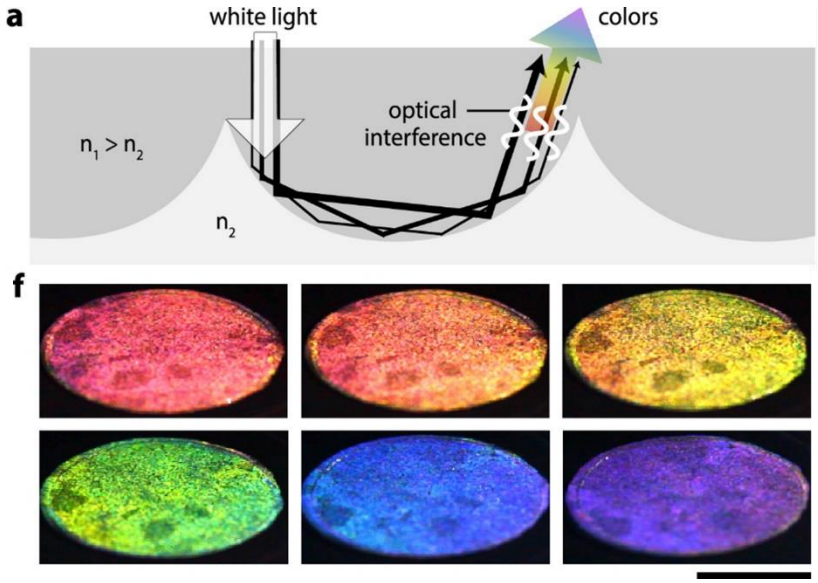

Figure 12. Top image – a schematic of total internal reflection at a concave interface. Bottom image – colors of the structures at different viewing angles. Figure reproduced from Goodling et al. (2020).

To provide a simplified quantitative description of the mechanism, a cylindrical, rather than spherical, geometry was considered [6]. The light source would be perpendicular to the direction of the cylinders, so only the light trajectories in that 2D plane would need to be

modeled [6]. This description is sufficient, as the equations are only provided to show quantitative support and will not be necessary for calculations in later chapters of this thesis. Furthermore, the bulk of the work in this thesis was done using cylindrical structures, so this model is sufficient.

The path length of each light ray can be calculated using equation 7 [6], where m is the number of bounces, R is the radius of curvature, and α_m is the local angle of incidence, given by equation 8 [6]. The intensity of the light at fixed incident and observation angle can be calculated by equation 9, where A_m is the amplitude, r_m is the complex Fresnel coefficient, n_1 and n_2 are the refractive indices of the higher and lower refractive index media respectively, and λ_0 is the wavelength of the incident light [6].

$$l_m = 2mRcos(\alpha_m) \quad (Eq. 6)$$

$$\alpha_m = \frac{\pi}{2} - \frac{\pi - \theta_{in} + \theta_{out}}{2m} \quad (Eq. 7)$$

$$I = \left| \sum_{\substack{m \\ all\ possible\ paths}} A_m(\alpha_m)[r_m\left(\alpha_m, \frac{n_1}{n_2}\right)]^m \exp\left(\frac{2\pi i n_1}{\lambda_0} l_m(\alpha_m)\right) \right|^2 \quad (Eq. 8)$$

Initially, the color was observed in droplets with a Janus shape, illustrated in Figure 13. This shape provides the curvature necessary to support the trajectories of the rays that will interfere to give rise to the color [6]. In the work, the droplets were formed from two immisible

oils (a hydrocarbon and a fluorocarbon oil) and stabilized in a combination of Capstone FS-30 and Triton X-100 surfactants to create droplets where both oils would be partially stabilized in the aqueous phase, giving rise to the Janus morphology [6]. The curvature of the interface between the two oils can be tuned by changing the ratios of the surfactants, as each stabilizes one of the oils used [6]. Since the color results from light interacting with this interface, it will change as the curvature changes so that by the time a double emulsion droplet was formed, total internal reflection could no longer occur [6]. This aspect, as well as a demonstration of how two different colors can be produced side-by-side, is shown in Figure 14.

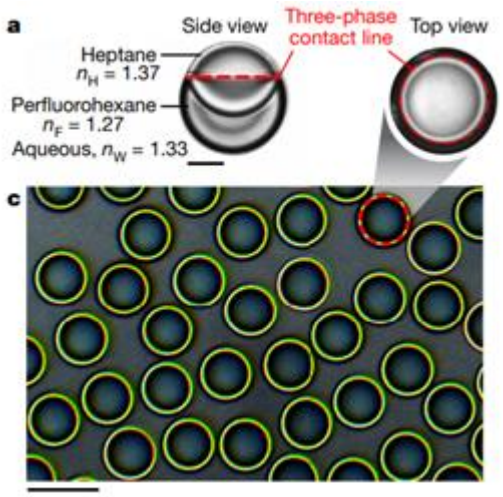

Figure 13. Janus shape of droplets and the three-phase contact line from which the color emanates, reproduced from Goodling et al. (2019).

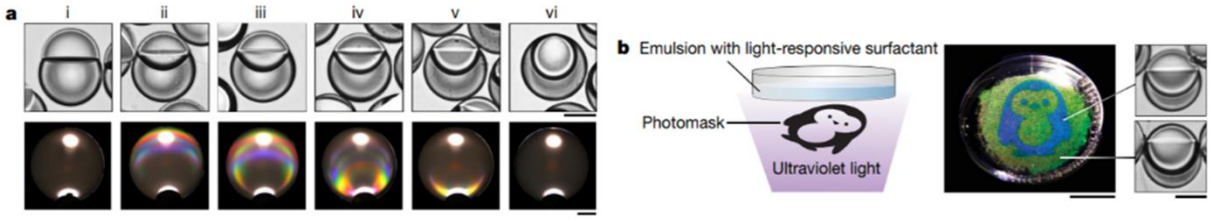

Figure 14. Demonstrating that a change in curvature affects the color pattern, reproduced from Goodling et al. (2019).

The necessary curvature can be replicated in polymer materials to create solid versions of the structural color [2]. A higher refractive index polymer is either backed simply in air ($n \cong 1$) or with a silicone ($n \cong 1.4$), where a silicone will provide a more vibrant color due to the smaller index contrast. The benefits of ease of reconfigurability and potential for stimuli response are lost in polymers, but stability and ease of fabricability are gained. Structural color via total internal reflection in both droplets and polymers will be explored in this thesis.

Due to the novelty of this mechanism of structural color, there is much fundamental knowledge about the mechanism to be discovered as well as many potential commercial applications to be explored. This thesis contributes to the fundamental knowledge of structural color at microscale concave interfaces as well as develops a commercial application utilizing the color.

Molecular modeling of surfactant molecules at an oil-water interface

Motivation

Microscale structural color can be produced and studied in multiphase droplets [6]. Initially, it was thought that only droplets with a Janus morphology could produce the color [6], but double emulsion droplets were shown to display color as well. Investigating the mechanism of structural color in double emulsion droplets is the topic of the following chapter in this thesis. To better understand the interactions between the surfactant, oil, and water molecules at the interface between the outer oil and aqueous phase in double emulsion droplets, a molecular model of the system was developed. Not only does this model serve as a visual aid, but it helps to provide an explanation for oil solubilization into the aqueous phase, which is an issue with droplets.

Development of the Model

The surfactant sodium dodecyl sulfate (SDS) was chosen to be modeled. Although Pluronic F127, a nonionic polymer oxide surfactant [15, 16], was typically used for the droplet experiments, it was determined that due to the long polymer chains with varying lengths [16], a different surfactant had to be modeled to create a feasible, easy to decipher graphic. Therefore, SDS was chosen instead due to the molecule's definite and relatively short length [17]. Like Pluronic F127 [16], SDS also has a hydrophobic and a hydrophilic end [17]. The difference is that SDS is an ionic surfactant [17], where the charged head sits in the aqueous phase. However, since both surfactants have oxygen atoms in their hydrophilic ends, and therefore would both

experience hydrogen bonding with the water molecules, SDS is an adequate replacement for Pluronic F127.

SDS at a toluene-water interface was modeled using CrystalMaker software. The atom coordinates were obtained from PubChem [17], and then the molecule was saturated with hydrogen atoms. In order to space the surfactant molecules accurately along the interface, the surface area coverage per SDS molecule was obtained from literature. This value, 71 $Å^2$, for SDS at a benzene-water interface [18] was used since there was no measured value for a toluene-water interface, and benzene and toluene only differ by a methyl group. The effective surface area that a single SDS molecule occupies on the interface was assumed to be circular, and the radius was obtained to be 4.75 Å. Therefore, the distances between surfactant molecules at the interface are 2r, which is equal to 9.51 Å. The molecules were moved 9.51 + r_{carbon} Å away from their original coordinates in either the y, z, or both y and z directions in CrystalMaker. The radius of carbon was added because there is a difference in distance, which is one carbon radius, between the distance along the interface between two carbons in the SDS molecules and the position in space that CrystalMaker assigns those carbon atoms.

To complete the model, water and toluene molecules were added. Again, the coordinates for toluene were obtained from PubChem [19], but the water molecule was manually drawn on CrystalMaker using data from Trolier-McKinstry and Newnham [20] since the coordinates were not available from PubChem. Then, the hydrogen bonds [20] between the hydrogen atoms of the water molecule and the oxygen atoms of the hydrophilic head of the SDS molecule were added and given a dashed bond to signify the hydrogen bond. The Van der Waals bonds [21] between

the carbon atoms in toluene and the carbon atoms in the hydrophobic tail of the SDS molecule were added and depicted with a dotted bond. Finally, to finish the molecule, the radii were changed to covalent radii using values from WebElements [22, 23, 24, 25] since SDS is a covalent molecule.

PowerPoint was then used to add a partial three-dimensional spherical surface to represent the droplet interface. The surface was chosen to reside between the hydrophilic head and hydrophobic tail of the molecule, since the water and oil would prefer those ends respectively. Two filled arc shapes were created and shaded with gradients to resemble a three-dimensional spherical interface.

Discussion of the Model

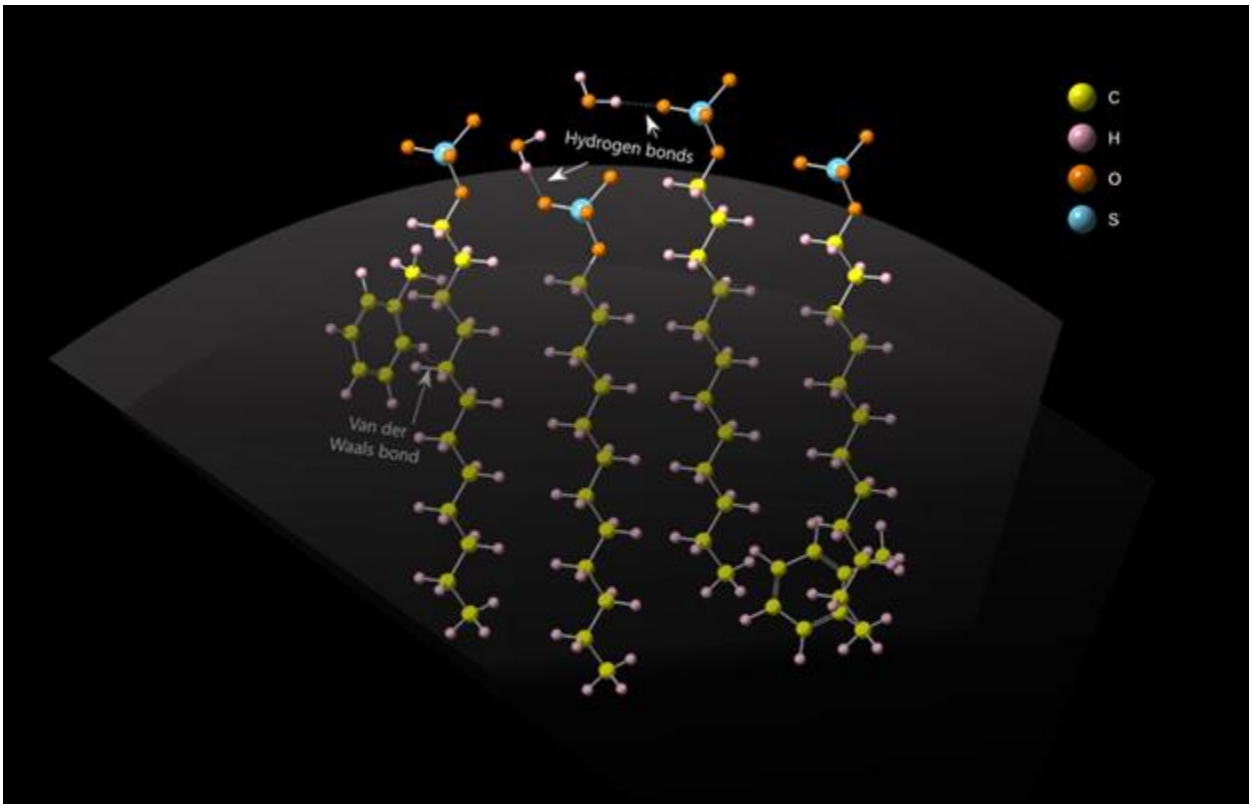

Figure 15. Full model depicting SDS molecules at a toluene-water interface.

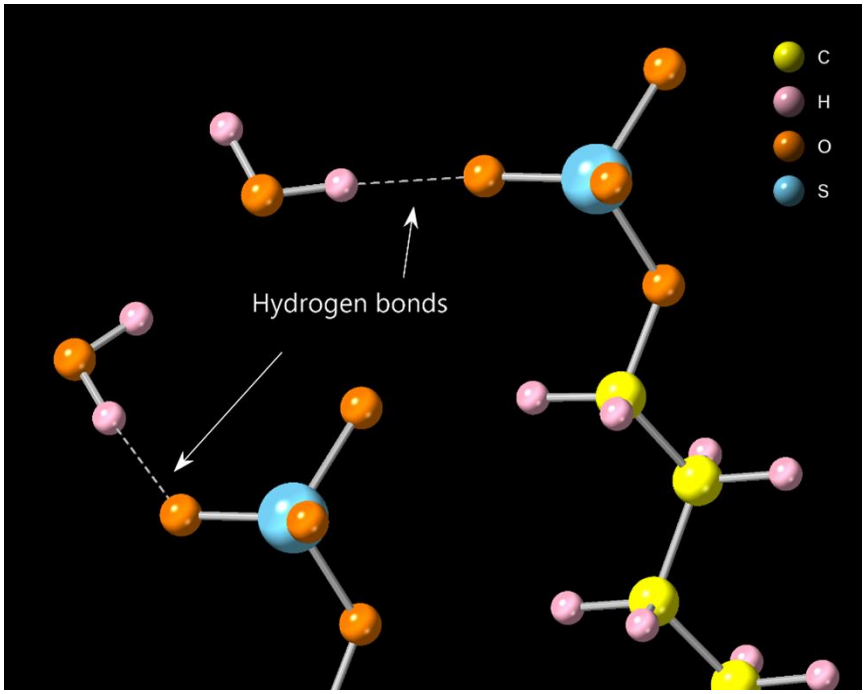

Figure 16. Magnified image of the hydrogen bonding between the oxygen atoms in the SDS molecules and the hydrogen atoms in the water molecules.

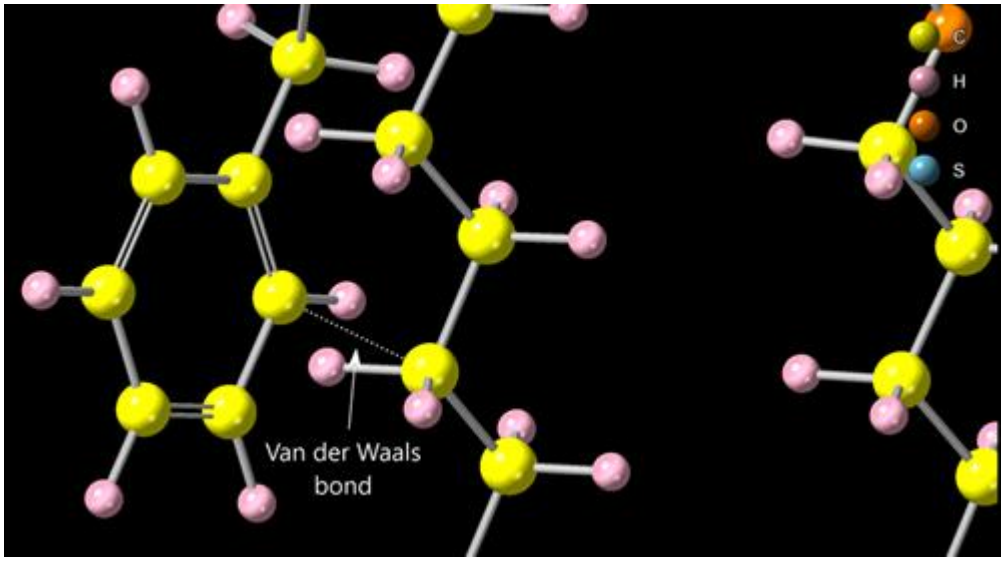

Figure 17. Magnified image of the Van der Waals bonding between a carbon atom in a toluene molecule and another carbon atom in an SDS molecule.

The model reveals that there are large spaces between surfactant molecules at the interface. It should be noted that the model assumes that the molecules are not dynamically repositioned to orientations not perpendicular to the interface and therefore remain fixed straight upward. The gaps between SDS molecules at the interface are larger than the toluene molecules, so the model supports the experimentally observed solubilization of toluene into the aqueous phase by visually depicting the relative sizes and spacing of the molecules. Although the toluene molecules experience Van der Waals bonding with the hydrocarbon tails of the SDS molecules, this type of interaction is quite weak [20] and therefore does not keep the toluene tightly bound to the droplet, further supporting the observed solubilization.

The interactions are also useful to see on the molecular level where the molecules are likely to be located at a given time. Although Van der Waals bonding is much less strong than hydrogen bonding [20], the molecules interact with the surfactant molecules at approximately the same bond distance [20, 21]. Overall, this model provides a deeper understanding for the research conducted on these droplets and the observed oil solubilization into the aqueous phase.

Conclusion

A molecular model of SDS surfactant molecules at a toluene-water interface was modeled using CrystalMaker software for the structures and PowerPoint for interface surface rendering. This model was created to visualize research on structural color in double emulsion droplets on the molecular level to gain a deeper understanding of the research. Additionally, the model will be used to direct future research. It has been revealed that the rapid solubilization of

toluene into the aqueous phase surrounding the droplet is likely due to the spacings between surfactant molecules at the interface. Therefore, an oil that is larger than the spacings between surfactant molecules should be chosen to avoid this solubilization. Once an adequate molecule has been found, it can be added to this model to visualize to determine if it should be tried experimentally. Because of this aspect, the model saves time and resources used since oils can be "tested" in the model before using the actual chemicals in lab. Therefore, the model benefits the research by providing a picture on the molecular level, which is not easily obtained in situ, and allowing the researcher to test potential oil molecules for the outer phase of the droplets without the waste and expense of laboratory resources.

Investigation of structural color in microscale double emulsion droplets

Motivation

As discussed in the first chapter, it was determined that the droplets would only display color if the droplet had a certain curvature, a Janus shape, that could support total internal reflection [6]. However, the color was also observed in double emulsion droplets, which have a much more severe curvature at the oil-oil interface. Therefore, the mechanism of this observed structural color was investigated. A new model was proposed as to the mechanism behind this observation, as well as measurements to obtain a better understanding how outer oil shell thickness and droplet morphology affect the color of the droplets. The hypothesis is that light, incident from below the droplet, passes through a lower refractive index oil to a higher refractive index oil and has total internal reflection along the water-outer oil interface. Furthermore, the total internal reflection, and therefore observed color, is dependent on the ratio of the two oils and droplet morphology. A schematic of this proposed mechanism is shown in Figure 18. It has been observed that as the toluene solubilizes into the aqueous phase, the droplets at first have no color, then have color that changes until the color again disappears.

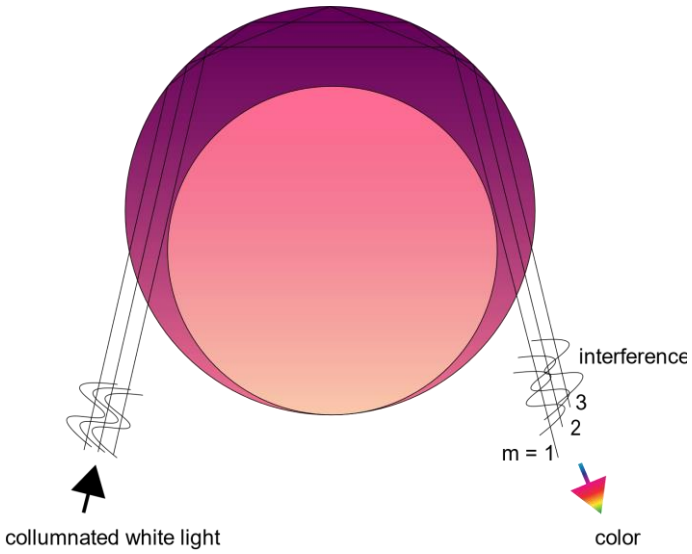

Figure 18. Proposed mechanism for the generation of structural color from double emulsion droplets.

Experimental

The droplets were formed in a Dolomite 100µm 3D flow focusing microfluidics chip, where the aqueous phase (channels 1 and 4) contained 0.1wt% Pluronic, the inner oil phase (channel 2) contained perfluorooctane, and the outer oil phase (channel 3) contained toluene with dissolved pyrromethene dye. The pressures were set so that the toluene had at least 50% less pressure than the perfluorooctane – these pressures ranged from 600mbar to 200mbar for the toluene, while the perfluorooctane was set to 1000mbar and the aqueous to 1500mbar. The reason for the range in pressures for the toluene was due to experimenting with the ratio of the two oils, but also that a pressure that would give the droplets color with one experiment would not give color for the next. This problem will be discussed in the following section.

Once the droplets were made, they were pipetted into a dish to be observed under both a transmission microscope as well as a Zyla inverted reflection microscope. The former would

verify, by shaking the dish, that the droplets were indeed double emulsion and not Janus. The latter verified that the droplets had color. If no color was observed, the sample would be left to sit until enough toluene had solubilized into the aqueous phase to support total internal reflection.

After verifying that the droplets displayed color, the dish would be carefully transported to a Leica Microsystems confocal microscope, where the droplets would be imaged at various depths through their z-axis. The argon and HeNe lasers were selected, and a wavelength of 514 nm was increased to 30% intensity (all others were 0%) [26, 27]. These settings were chosen to excite the fluorescent dye (pyrromethene) in the toluene phase [26, 28]. In order to obtain images at depths throughout the z-axis, the beginning depth was set to a point slightly below the bottom of the droplet and the end to a point slightly above. Then, the number of steps (where images would be taken) was set to 100. The distance between steps was not relevant to imaging itself, however, was necessary in creating the TIFF stack of images in order to obtain an accurate 3D image of the droplets for further analysis.

Results and Discussion

Before discussing the results of the experiments detailed above, it is worth noting that other combinations of oils were tested and considered for imaging through the confocal microscope. The process for ultimately choosing toluene and perfluorooctane for the experiments will be mentioned here briefly.

Due to the densities of the oils, the higher refractive index sat at the top of the droplet so that in order to observe iridescence, the incoming light would have to be incident from below the droplet instead of from above, which is the direction from which light naturally emits. Therefore, a combination where the denser oil has the higher refractive index would be more desirable. Also, toluene rapidly solubilizes into the aqueous phase, so an outer oil that does not solubilize as quickly would provide more accurate results. After testing various pairs of oils, hexachlorobutadiene (denser, higher refractive index) and 1-ethoxynonafluorobutanes were chosen [29]. However, when the droplets were imaged under the confocal microscope, both phases displayed fluorescence, meaning that the dye had solubilized into the inner oil phase. It was determined that since the mechanism of the toluene-perfluorooctane droplets was the same, those oils could be used for imaging as long as the dye remained in the toluene phase, which it did. Therefore, the initial combination of oils was ultimately used for the experiments.

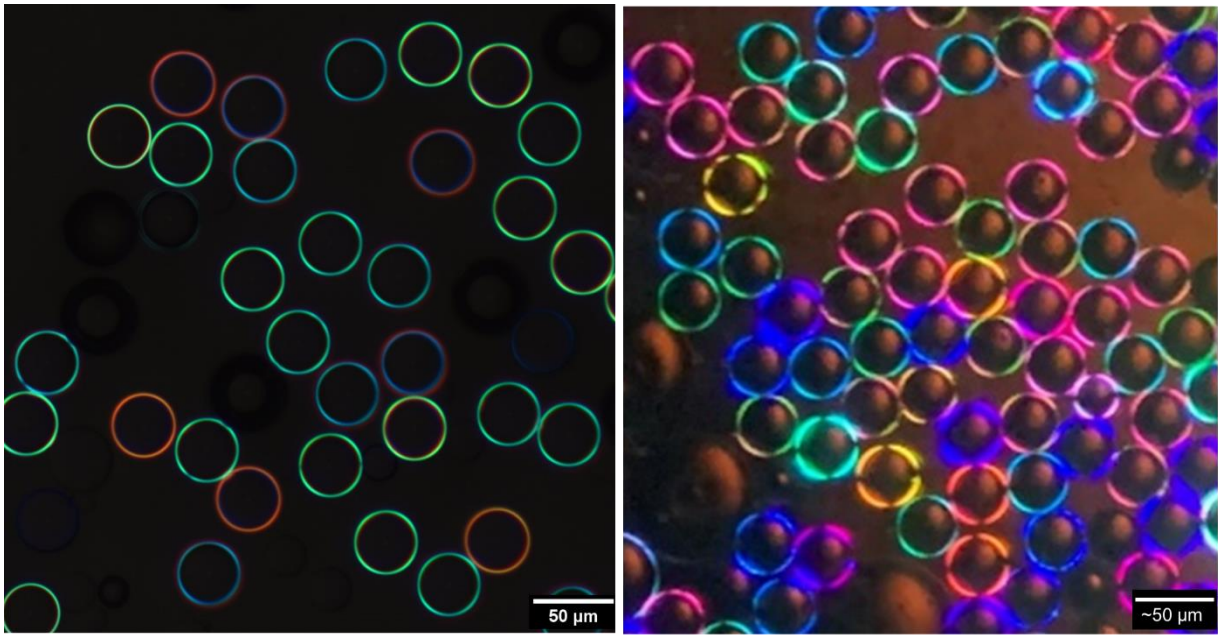

Figure 19. Reflection microscopy images of a. hexachlorobutadiene and 1-ethoxynonafluorobutanes droplets and b. toluene and perfluorooctane droplets exhibiting structural color.

Imaging using the confocal microscope presented some issues that had to be resolved. Since the microscope could not show the reflected color, there was no way to verify those optical effects at the confocal itself. However, steps were taken to verify the color through the reflection microscope then immediately, and carefully, without moving the droplets in the dish, transport the sample to the confocal. Therefore, there is high confidence that the images taken were of droplets that were experiencing total internal reflection. Also, the droplets often tended to drift in the dish, resulting in a shifted droplet image, which did not give an accurate 3D representation of the droplet. Since there was no way to keep the droplets still, and continuing to create samples that inevitably would not be imaged cost time and money, these experiments were ultimately halted.

However, there was one successful TIFF stack of the droplets created, shown in Figure 20, that will be analyzed. To create the three-dimensional image, the stack of images from the confocal microscope was loaded into ImageJ software, where a 3D Project was created of the images. As expected, there was fluorescence (again, the dye was dissolved into the toluene phase) observed as a thin shell around the droplet, with most of the volume at the top of the droplet. What was not expected, though, was that the brightest fluorescence was in a ring around the circumference of the droplet. This location was where the ring of color had been observed in the reflection microscope, not at the top of the droplet where most of the volume of the toluene resided. One theory is that the emitted light from the laser was being total internally reflected at the toluene-water interface, which would explain the intensity difference around the circumference of the droplet. However, the emission wavelengths (555-667nm) were selected so that no reflection from the laser would be registered [27]. Another theory is that the emitted wavelengths interacted with the interface, which is unlikely, since the light rays would not be entering into the droplet and allowed to totally-internally reflect. Regardless, measurements of the toluene thickness could still be taken, which are recorded in Table 1. Where the measurements were taken is shown in Figure 21.

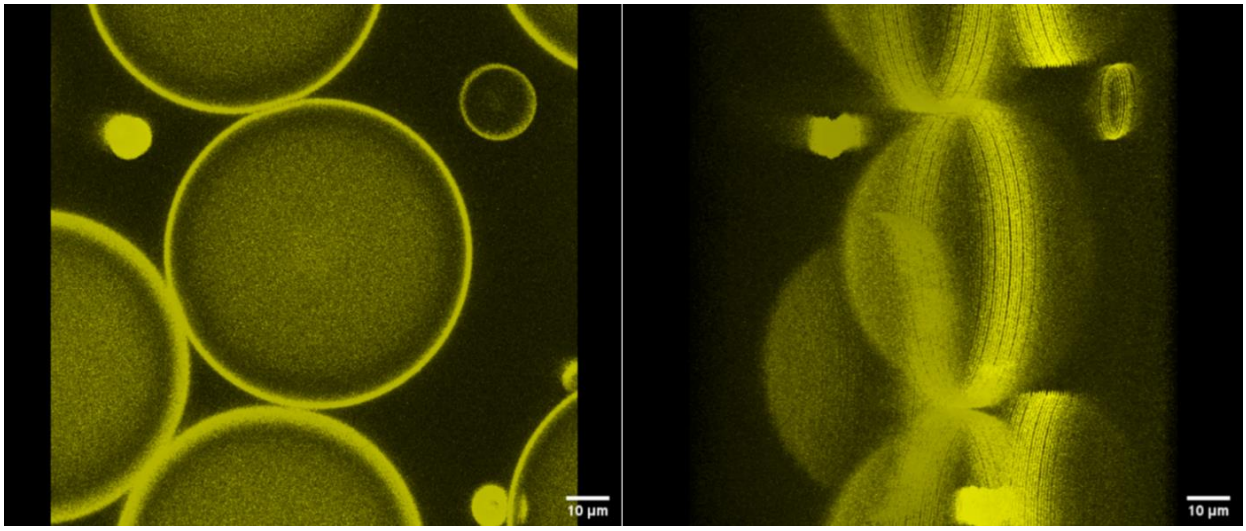

Figure 20. 3D images of the droplets shown in plane and rotated about the y-axis.

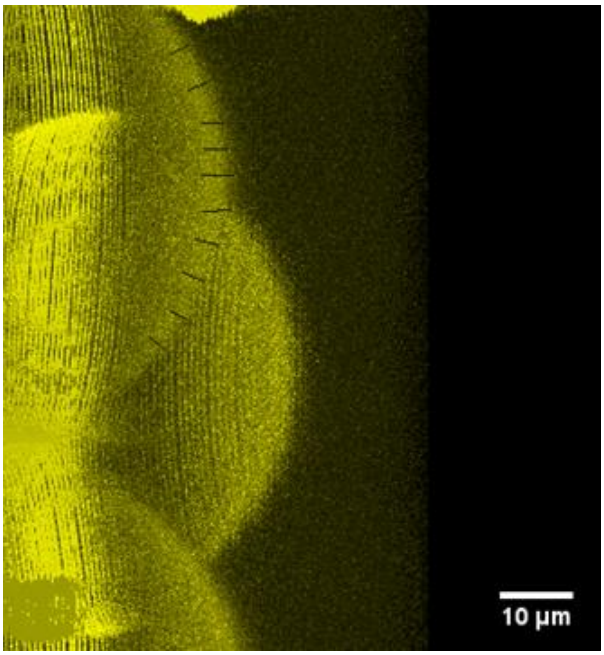

Figure 21. Measurements (shown as black lines) of the outer oil shell thickness.

Table 1. Measurements of the outer oil shell thickness.

Measurement	Width of Shell (μm)
1	3.992
2	2.818
3	3.624
4	2.421
5	2.731
6	3.048
7	3.162
8	2.529
9	2.477
10	3.053
Average	2.986
	Diameter of Droplet (μm)
1	70.684
2	70.449
average	70.567

The thickness measurements were taken using ImageJ. The 3D image was rotated just shy of 90 degrees about the y-axis to allow for the clearest perspective for measuring the thickness. The average thickness was found to be 2.986 μm, which is only 4.23% of the total diameter of the droplet. Therefore, it can be concluded that only a thin shell of the higher refractive index oil will support total internal reflection and result in color.

Conclusion

Double-emulsion droplets were not expected to display structural color due to their severe curvature, yet the color was still observed. A model for the mechanism was proposed, where the total internal reflection would be occurring at the interface between the high refractive index oil and the aqueous phase. The outer oil “shell” was found to be 2.986 μm thick, which is

only 4.23% of the diameter of the droplet. Therefore, only a very thin shell of the outer oil can create the observed color.

There also were obstacles during the project which rendered it not feasible for further study. The microfluidics chip would often become clogged with small fibers, which were challenging and time-consuming to remove. Also, the droplets tended to drift in their dish of aqueous media during the imaging using the confocal microscope. Therefore, inaccurate 3D images would be obtained. This process would result in wasted time, materials, and money. The solution to these problems is to study structural color via total internal reflection in polymer substrates.

Development of an inkless printing technique for use on polymer iridescent substrates

Motivation

Although droplets have some desirable properties, i.e., reconfigurability, ability to study color change over time due to solubilization, and ability to create the specific curved interfaces that support structural color, their problems outweigh these benefits. To achieve monodisperse droplets, which is necessary to obtain uniform color across all the droplets in a dish, microfluidics must be used. These devices are small glass chips with channels on the microscale. These channels, due to their small size, can easily become clogged, which also means that they are difficult to become unclogged. Another issue with droplets is that their outer oil can solubilize into the aqueous phase. As seen in the second chapter, there is much space between surfactant molecules at the oil-water interface, so oil molecules can easily escape. As the outer oil solubilizes, the color of the droplet changes until no more color appears. This behavior makes measurements and observations difficult with the potential for considerable error. Therefore, the focus was shifted to study microscale structural color in solid polymer microstructures. The advantages to these structures over droplets are ease of fabricability and characterization. Solid structures have a wide array of uses, such as those for aesthetic and product design and security features.

The polymer microstructures can be fabricated in thermoplastic polymers, which deform and soften under heat. Since the color is dependent on the structure, a change in the structure, whether that be width, height, or contact angle, should result in a change in the color. Therefore,

if heat is used to deform the microstructures, the color is expected to change. One way to introduce heat is via an infrared laser, which also provides the ability to "write" on the samples. This chapter will explore the precision and limitations of using an infrared laser to print on structurally colored samples, characterize the induced deformation, and discuss the implementation of this printing process in an industrial setting.

Experimental

The polymer iridescent substrates were formed from replications of an original master mold. Grayscale lithography was used to create the microstructures on a silicon wafer. Then, an initial silicone mold was created from the master mold, followed by a second silicone mold to use for further replication into polymers. Mold Star silicone was used, and its refractive index was measured to be 1.41. This mold is useful to allow the polymer to be easily removed from the mold and to not degrade the master mold over many future replications. The polymer, which is a square of polyethylene terephthalate glycol (PETG), was placed on top of the silicone mold and into an oven for 8 hours at 130 °C. This temperature is above the glass transition temperature yet below the melting temperature of PETG, as the sample only needs to become soft to take on the imprints of the structures. Once cool, the square would be peeled off the silicone mold to reveal iridescence. This process is illustrated in Figure 22.

A Full Spectrum Laser hobby series CO_2 laser cutter with corresponding Retina Engrave software was used to thermally deform the structures. The PETG sample was placed inside the chamber, structure side up, with the cylindrical structures running horizontally. This orientation

of the structures ensures that both the deformation and cylinders are running perpendicular to a cross-sectional cut, which is made to characterize the structures. To conduct basic trials of laser parameters, simple horizontal lines were created in the “design” tab. To create the proof-of-concept prints, the text feature was used to print “Zarzar Lab”, and a vector image of a heart was loaded into the software to print the heart image. The design would then be rendered to the raster engrave and vector cut modes, where the user would decide which mode to use to print the design. For each mode, multiple laser parameters could be modified; the effects of these parameters will be discussed in the next section. To make the print, the laser head was moved to a place on the sample, and the “play” button was pressed.

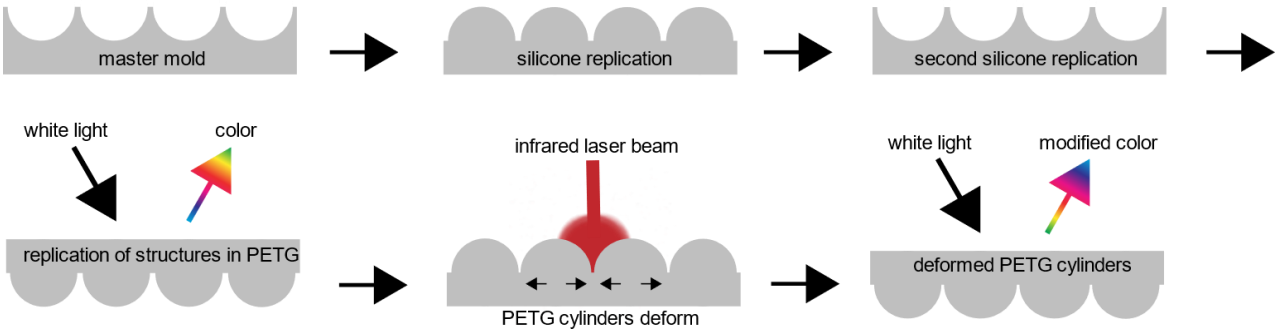

Figure 22. Schematic of the process for fabricating and deforming the polymer microstructures.

The induced deformation was measured with a Sensofar S Lynx optical profilometer with corresponding SensoSCAN software using 50x interferometry. Additionally, a cross-section method was used. Moldstar silicone mixed with a black silicone pigment was prepared and placed onto the structure side of a PETG sample only where the deformation occurred. Next, silicone (without pigment) was prepared and poured on the back of the whole sample. After curing, box cutters were used to cut through the silicone perpendicular to the lines of

deformation into a thin strip, shown in Figure 23. The cross-section of the structures was then viewed under a Zyla optical microscope, where the black marks indicate where deformation has occurred. ImageJ software was used to measure the height and width of the structures.

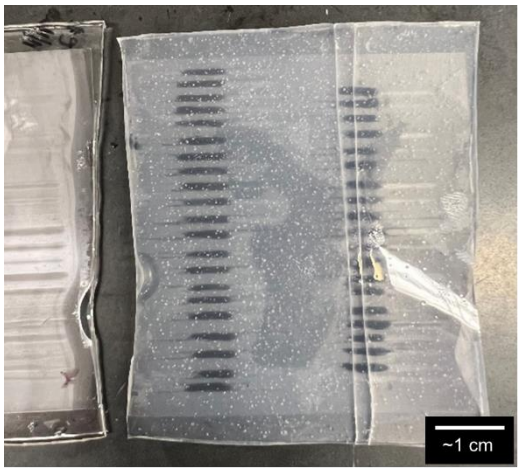

Figure 23. Phone camera image of silicone with deformation marked and a cross-section piece cut.

To image the samples, the same black silicone mixture was poured on the structure side to enhance the color. A Canon EOS Rebel T6 DSLR camera was positioned above the sample, and images were taken as the sample was rotated in the plane of the table.

Results and Discussion

The main result found is that infrared lasing can be used to modify the color of thermoplastic polymer iridescent substrates. Within that result are others concerning limits of the process, effects of changing the laser parameters, and measured deformation. Each of these results will be discussed and used to provide an outlook on implementing this process in an industrial setting.

Modifying Color

As mentioned in the experimental section, straight lines were printed on the samples to test varying the laser parameters. By using a design that only involves one pass over a region, each parameter can be independently tested without the influence of previous lasing. The first method that was tested was raster engrave, which is typically used to lase over areas. The two parameters that can be modified are raster speed and raster power. Decreasing the speed completely destroyed the color, so it was determined to not be a viable parameter to use and test. Therefore, only raster power was tested. The power was increased by 1% for each line until color was no longer observed. The color began to change at 23% vector power and was gone at 65%. Since there was not much visual change over most of the power range, only the low and high raster power lines are included, which is shown in Figure 24.

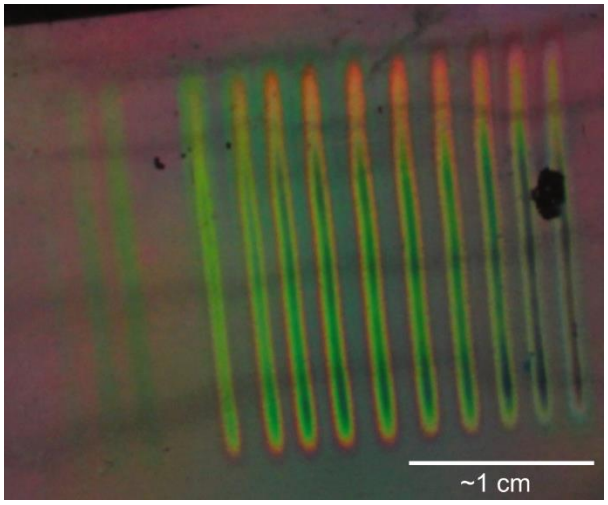

Figure 24. Lines drawn in raster engrave mode. The first three lines beginning on the left are 23-25% raster power, then the next lines are 51-65% raster power.

Upon analyzing Figure 24, 25% raster power should be the lowest power used, as 23-24% are too faint to be easily seen. Also, the 25% raster power appears to only have one color in the lased area, while the higher powers appear to have a different color along their edges. This edge color is likely the result of thermal energy transfer to the area directly surrounding the lased area. This observation would give a user an additional "color" to choose from when printing.

Next, vector cut was tested. This mode is typically used to trace an outline of an object. The parameters for this mode are speed, power, number of passes, and vector current. Speed was again not tested due to the same reason mentioned earlier. The first parameter tested was power (number of passes set to 1; vector current set to 100%), and it was found consistently that 0.2 power was required to modify the color. For the sample used for deformation measurements, 10 power was found to be the point at which color no longer appeared. Although the lowest power needed for deformation did not change from sample to sample, the point where no color could be observed did. The likely reason for this discrepancy is that the samples differed in structure size, so samples with larger structures would lose their color more rapidly than those with smaller structures. The reason that 0.2 power was consistent is that the polymer needs enough thermal energy from the laser to overcome its glass transition temperature, and hence, to deform. Therefore, this observation is due to the intrinsic material more so than the lasing process, so it is expected to be consistent across all PETG samples. The effect of changing the laser power is shown in Figure 25.

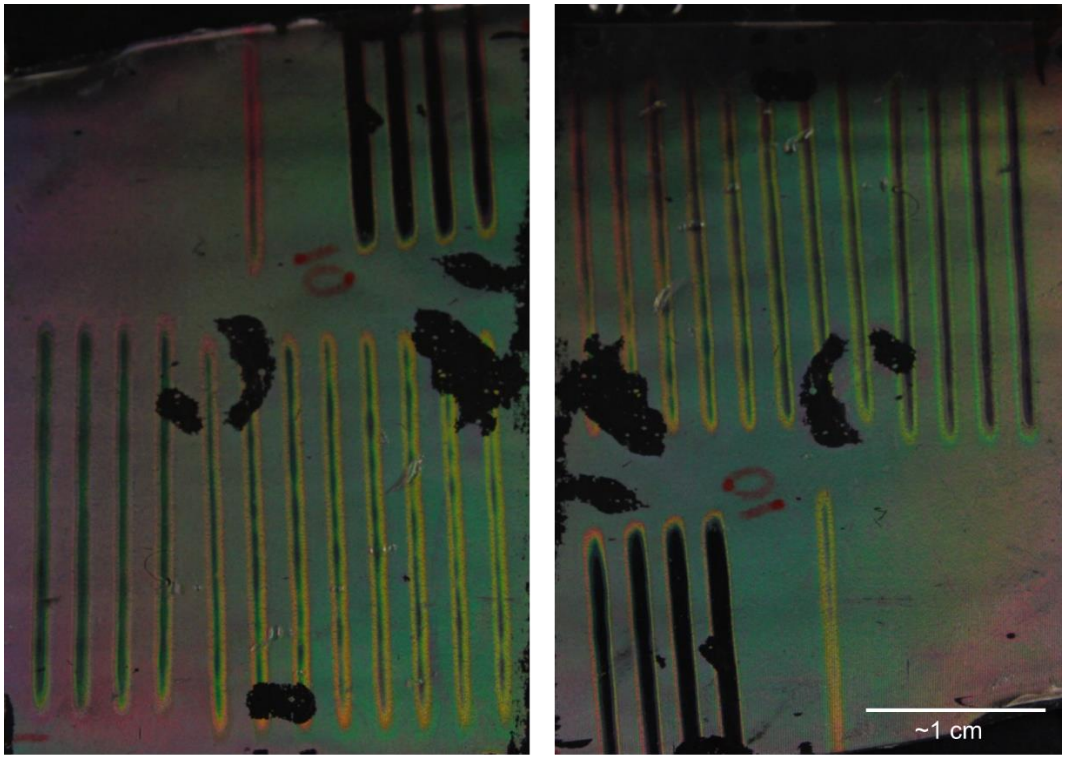

Figure 25. Lines drawn in vector cut mode. The line drawn with 0.2 power is shown to the left of the line with no color (in the left image). The right image is the same as the left, just rotated 90° in the plane.

The next parameter tested was number of passes, which is shown in the top three lines in the images of Figure 26. The vector power was set to 0.2 and the vector current to 100% as controls. By three passes, color can no longer be observed. This parameter appears to have the greatest effect on the color, which is likely due to lasing over an area that already has deformation. Therefore, this parameter is the most effective at removing the color. The user can be assured that by three passes, the color will be gone.

The last parameter tested was vector current, which appears to be a way to deliver even less thermal energy to the sample than a set power can, as the vector current was set to 100% for the control. With a laser power of 0.2, as low as 75% vector current can be used to generate a

color change. Modifying this parameter is shown in the bottom six lines in the images of Figure 26 and can be used to provide the user even greater control over the desired prints. The similar appearance of only one color in the line, as observed in very low raster engrave powers, is observed here as well. As vector current is increased, a secondary color along the edges of the lines begin to appear.

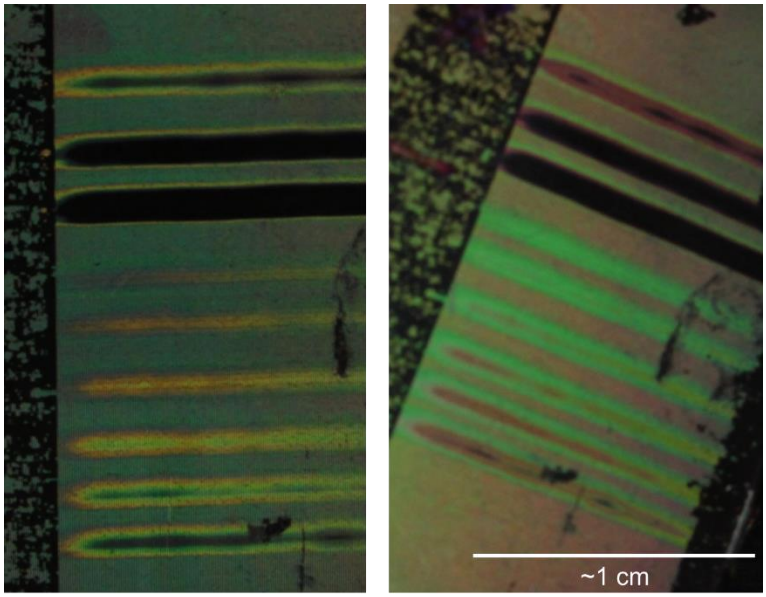

Figure 26. The first three lines are increasing passes from 1-3. The following six are increasing vector current from 75-100% in increments of 5%.

Measuring the Deformation

It is of interest now to quantify the induced deformation. The cross-sectional area method will first be discussed, as it is the standard method in the Zarzar lab used to characterize these structures. The heights and widths of the unlased structures, lased structures at 0.2 vector power, and lased structures at 10 vector power were measured. There was no measurable deformation at 0.2 vector power, which was surprising, as the observed color had changed. For the 10 vector

power, however, there was a change in structure width of 4 μm and height of 12 μm. Also, the structures lost their distinct edges and appeared almost sinusoidal, without clear boundaries between structures. The cross-sectional area images are shown in Figure 27. Example measurements of the deformed structures are shown in Figure 28.

Profilometry measurements were conducted on raster engrave samples with a raster power of 32%. These images are difficult to obtain, as the structure heights are often too deep for the tool to analyze. Therefore, the line with 32% was the first line shallow enough to be measured. There was no change in height, but a change in width of 1.7 μm was observed. This measurement stands in contrast to the one obtained using the cross-sectional method. Two potential reasons are that this is not an accurate comparison of laser powers and that profilometry is more precise. Additionally, 1.7 μm is very close to the standard deviation of structure sizes found using the cross-section method, so it could be true that the measured deformation using profilometry is not significant. A profilometry image of the measured line is shown in Figure 29.

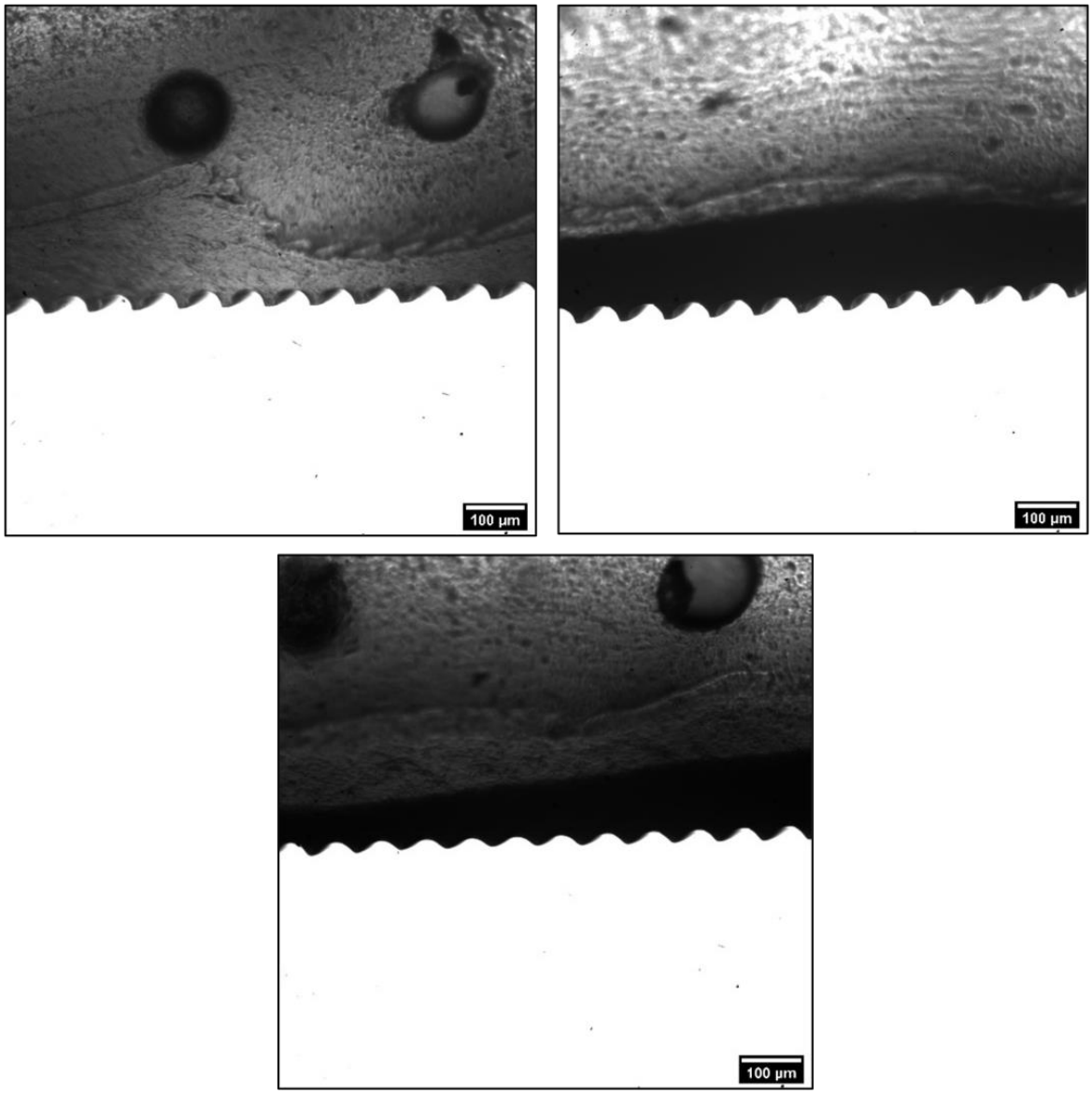

Figure 27. Cross-section images of the (clockwise from top left) unlased structures, 0.2 vector power, and 10 vector power.

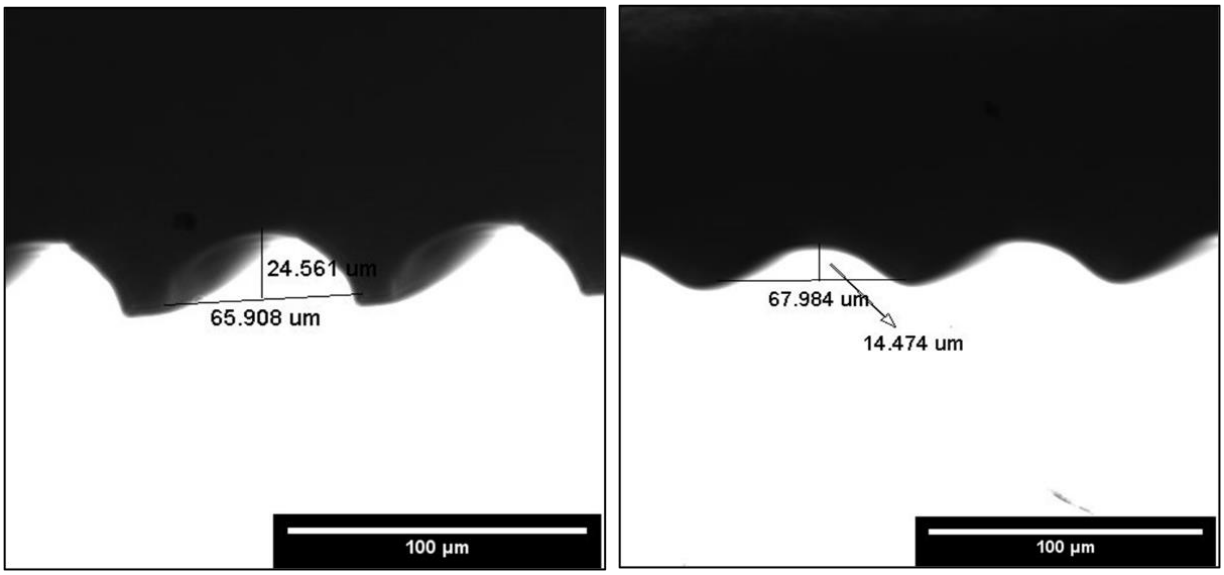

Figure 28. Close-up images of the lased structures showing how their heights and widths were measured.

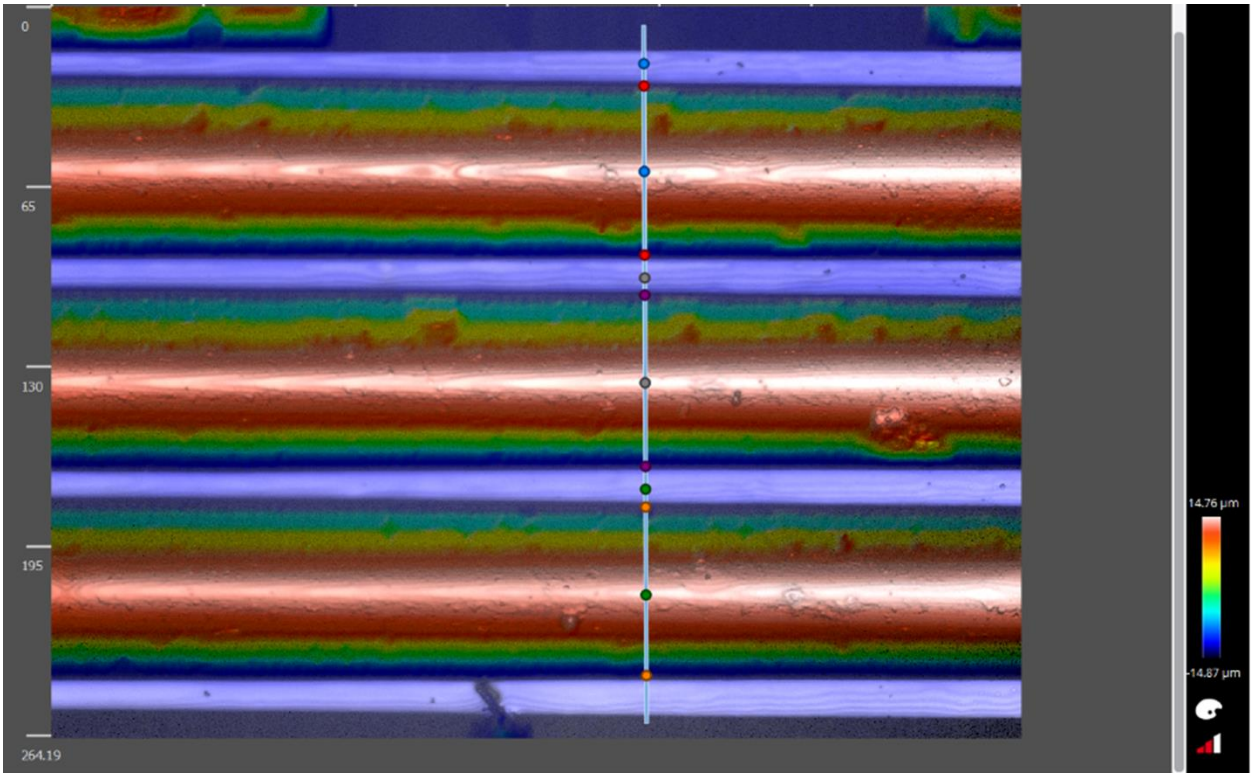

Figure 29. Profilometry image of lased structures.

Considerations for Industry Use

Those wanting to implement this technology in industry likely will not care as much about how much deformation has occurred. Instead, they will want to know how much control they will have over the process. Drawing a conclusion from the results above, there are four "colors" that can be utilized in a design/print – the original sample color, one color, one color with a different edge color, and no color. In the vector cut mode, power, current, and number of passes can be modified; in the raster engrave mode, only power can be modified. Therefore, more control can be exhibited with vector cut over raster engrave. However, if the user wants to lase an area, raster engrave must be used, although lasing areas completely ablates the color due to thermal conduction into the surrounding areas. Figure 30 shows a vector image of a heart printed in two orientations using raster engrave, and Figure 31 shows the text "Zarzar Lab" printed using vector cut. These images serve as proof-of-concept prints.

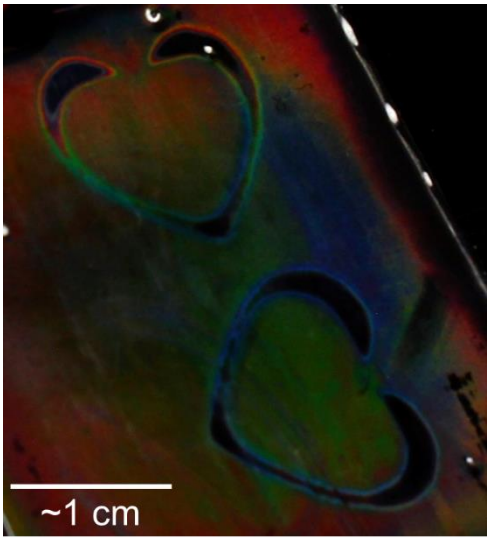

Figure 30. Vector image of a heart printed on a structurally colored sample; vector image obtained from VectorStock.

Figure 31. The text "Zarzar Lab" printed onto a structurally colored sample shown from two orientations.

Conclusion

Low-power infrared lasing was found to modify the color of thermoplastic polymer samples exhibiting microscale structural color. This phenomenon can be used to create an inkless printing process for applications in design and security features. The limits and control of the process were determined through testing the laser parameters of power, current, and number of passes. The color can either be modified, modified with a different edge color, or completely removed. The induced deformation when the color first begins to change is below the variation of the sizes of the structures, but a structure width change of 4 μm is sufficient to remove the color. Proof-of-concept images were also provided to show industrial promise for the technology.

BIBLIOGRAPHY

[1] S. Kinoshita and S. Yoshioka, Structural Colors in Nature: The Role of Regularity and Irregularity in the Structure, *ChemPhysChem*, 6, 1442-1459, 2005.

[2] A. E. Goodling, S. Nagelberg, M. Kolle, and L. D. Zarzar, Tunable and Responsive Structural Color from Polymeric Microstructured Surfaces Enabled by Interference of Totally Internally Reflected Light, *ACS Materials Letters*, 2, 7, 754-763, 2020.

[3] S. Kinoshita, S. Yoshioka, and J. Miyazaki, Physics of structural colors, *Reports on Progress in Physics*, 71, 2008.

[4] M. F. Land, The Physics and Biology of Animal Reflectors, *Progress in Biophysics and Molecular Biology*, 1972.

[5] D. Jaszkowski and J. Rzeszut, Interference colours of soap bubbles, *The Visual Computer*, 19, 252-270, 2003.

[6] A. E. Goodling, S. Nagelberg, B. Kaehr, C. H. Meredith, S. I. Cheon, A. P. Saunders, M. Kolle, and L. D. Zarzar, Colouration by total internal reflection and interference at microscale concave interfaces, *Nature*, 566, 523-527, 2019.

[7] C. Palmer and E. Loewen, Diffraction Grating Handbook (sixth edition), *Newport Corporation*, 2005.

[8] E. G. Loewen and E. Popov, Diffraction Gratings and Applications, *Marcel Dekker, Inc.*, 1997.

[9] E. Yablonovitch, Photonic Crystals: What's in a Name?, *Journal of Modern Optics*, 1994.

[10] S. R. Hetzler, Infrared Optical Studies of HgTe-CdTe Superlattices and GaAs, *California Institute of Technology*, 1986.

[11] K. Sakoda, Optical Properties of Photonic Crystals, *Springer*, 2005.

[12] R. M. Drake and J. E. Gordon, Mie scattering, *American Journal of Physics*, 53, 1985.

[13] T. Wriedt, Mie Theory: A Review, The Mie Theory, *Springer Series in Optical Sciences*, 2012.

[14] P. Laven; Rainbows, Coronas and Glories; The Mie Theory; *Springer Series in Optical Sciences*; 2012.

[15] National Center for Biotechnology Information. Poloxalene. *PubChem.* https://pubchem.ncbi.nlm.nih.gov/compound/24751.

[16] *Biological Structures.* Ottenbrite, R.M. and Javan, R. s.l. : Elsevier, 2005.

[17] National Center for Biotechnology Information. Sodium dodecyl sulfate. *PubChem.* https://pubchem.ncbi.nlm.nih.gov/compound/3423265.

[18] Rosen, Milton J. *Surfactants and Interfacial Phenomena.* s.l. : John Wiley & Sons, 2004.

[19] National Center for Biotechnology Information. Toluene. *PubChem.* https://pubchem.ncbi.nlm.nih.gov/compound/1140.

[20] Trolier-McKinstry, Susan and Newnham, Robert E. *Materials Engineering.* s.l. : Cambridge University Press, 2018.

[21] Winter, Mark. Carbon: radii of atoms and ions. *WebElements.* https://webelements.com/carbon/atom_sizes.html.

[22] —. Hydrogen: radii of atoms and ions. *WebElements.* https://webelements.com/hydrogen/atom_sizes.html.

[23] —. Carbon: radii of atoms and ions. *WebElements.* https://webelements.com/carbon/atom_sizes.html.

[24] —. Oxygen: radii of atoms and ions. *WebElements.* https://webelements.com/oxygen/atom_sizes.html.

[25] —. Sulfur: radii of atoms and ions. *WebElements.* [Online] https://webelements.com/sulfur/atom_sizes.html.

[26] “Imaging with One Dye.” Leica Microsystems.

[27] Gregg, Amanda. “Experiment_Series025_Properties.” Penn State University, 28 Jan. 2020.

[28] “PYRROMETHENE 650 .” Exciton, 11 Apr. 1994.

[29] Zarzar, Lauren. “Organic and Fluorinated Liquid Combinations.”

ACADEMIC VITA – AMANDA GREGG

Education

The Pennsylvania State University
Bachelor of Science in Materials Science and Engineering
Schreyer Honors College
May 2022 Graduation

Research Experience

Zarzar Research Group at Penn State
Advisor: Dr. Lauren Zarzar
6/19-5/22
Droplet work:

- Investigated the mechanism by which color was appearing in double emulsions, as the geometry of these droplets should not support the total internal reflection necessary to produce structural color
- Using emulsions of a rapidly solubilizing outer oil, observed that the color changed with thickness of the outer oil
- Utilized confocal microscopy to create 3D images of the droplets to determine the shell thickness necessary to produce color

Polymer Microstructure work:

- Developing an inkless printing process for use on thermoplastic polymer iridescent substrates, where the iridescence results from the total internal reflection of light along concave microstructures
- Quantified that the change in the color pattern induced via deformation from low-power infrared lasing resulted in a change in microstructure width of 1-2 μm
- Evaluating the limits of control on deformation that can be induced by modifying parameters in the laser cutter software to determine the precision with which the color can be tuned

THRED Group at Penn State
Advisor: Dr. Christopher McComb
REU: 6/20-8/20

- Implemented natural language processing to visualize the similarities between scientific papers as points on a plot with the goal of locating relevant scientific literature more efficiently
- Programmed code in MATLAB that first conducts latent semantic analysis on the literature then quantitatively plots the papers based on their relative semantic similarities

Continuing research: 9/20-5/22

- Enhanced my program by calling the arXiv API to provide the literature and converting the program to a GUI that allows the user to search the API, interact with the plot, and save papers of interest
- Designed my program with an emphasis on ease of use, which I tested through pilot

studies
- Conducting human subjects research on the effectiveness of the GUI for locating more relevant literature in a shorter amount of time as compared to traditional methods for literature searching

Internship Experience

Parker LORD-Adhesives and Coatings Technology
6/21-8/21

- Evaluated the performance of low-VOC formulated adhesives through ASTM D429 Method B to meet environmental regulations
- Investigated the robustness of the primer/adhesive system for tank lining applications to determine application thickness ranges for optimal bond performance (evaluated through ASTM D429 Method E adhesion testing)
- Generated adhesive physical property, application, and bond strength data to improve the quality and accuracy of product technical data sheets
- Collaborated with a cross-functional team of distribution partners, application engineers, product development chemists, and customers

Honors Projects

Introduction to Materials Science
Advisor: Dr. Robert Allen Kimel
Fall 2019

- Researched the properties of the brass compositions used in musical instruments to connect concepts discussed in class to my passion for playing saxophone
- Planned and recorded lecture videos on the topics of solid solubility and structure, diffusion, mechanical properties and processing, and optical properties of the brasses

Crystal Chemistry
Advisor: Dr. Susan Trolier-McKinstry
Fall 2020

- Modeled surfactant molecules at the oil-water interface of an emulsion in CrystalMaker to gain a molecular-level understanding of my experimental work in the Zarzar lab
- Used data in literature to place sodium dodecyl sulfate molecules at the droplet interface and to add Van der Waals interactions of the toluene and water molecules to the surfactant molecules

Honors and Awards

Awards
Dean's List
Fall 2018, Spring 2019, Spring 2020, Fall 2020, Spring 2021, Fall 2021

Placed 2nd in the 2021 Materials Engineering Methodology and Design Competition for our team's project proposal Photocatalytic Carbon Negative Concrete for Building Sustainable Cities

Scholarships
4-Year
2018-2022

- Academic Excellence (through the Schreyer Honors College)
- University Park 4-Year Provost Award

College of Earth and Mineral Sciences

- Matthew J Wilson Honors Scholarship
  2018-2019
- Wheatall Earth & Mineral Science Award
  2019-2020
- E F Schulze Scholarship
  2020-2021
- Jane and Don Strickler Honors Scholarship
  2021-2022

Department of Materials Science and Engineering

- Perrotta Science and Engineering Scholarship
  2018-2019
- George & Madelein Todd Scholarship
  2019-2020
- Floyd A Hummel Jr. Scholarship
  2020-2021
- Penn State Metallurgy Alumni Scholarship
  2021-2022

Campus Involvement

Outer Dimensions Jazz Ensemble
Fall 2019, Fall 2021, Spring 2022
Keramos National Professional Ceramics Engineering Fraternity
2/20-5/22
Part-Time Grader
8/20-5/21; 1/22-5/22
Material Advantage
9/20-5/22
Fashion Society of Penn State
10/20-5/22